

Axisymmetric Vehicle Nose Shape Optimization

Vladimir Balabanov*

*Vanderplaats Research & Development, Inc., 1767 South 8th Street, Colorado Springs, CO 80906
(Currently at Boeing, 3003 W Casino Rd, Everett, WA 98204-1910, Mail Code 03-JP)*

Steven Young[†] and Stephen Hambric[‡]

Applied Research Laboratory, Pennsylvania State University, State College, PA 16804-0030

Timothy W. Simpson[§]

Pennsylvania State University, 314D Leonhard Building, University Park, PA 16802

Nomenclature

All the dimensions are provided as a fraction of the vehicle body radius.

x	– the rotational axis along the vehicle length
s	– the arc length along the cross section of the vehicle body starting from the center of the vehicle nose
$t(s)$	– the point of transition from laminar to turbulent flow
$l(s)$	– the point of laminar separation
a	– the main axis of the ellipsoid defining the rounding of the vehicle nose
b	– the secondary axis of the ellipsoid defining the rounding of the vehicle nose
R_{nose}	– the vehicle nose radius
R_{body}	– the vehicle body radius
Re	– Reynolds number
C_p	– pressure coefficient
$C_{p_{min}}$	– minimum value of the pressure coefficient

I. Introduction

When designing an axisymmetric vehicle nose, multiple performance characteristics have to be considered to ensure mission success. A design configuration that optimizes one performance characteristic may be different from the configuration that optimizes the other characteristic. In this case the final design could be the configuration that minimizes conflicts between the multiple performance characteristics. The shape of the vehicle nose has a significant effect on some of the vehicle performance characteristics. This paper explores variations in the shape of the nose and how these shapes affect various performance characteristics.

II. General Problem Formulation

Figure 1 presents the schematic view of the upper half of a notional axisymmetric vehicle nose, similar to those investigated by Arakeri and Acosta¹. For our problem formulation the nose shape is controlled via the location of two control points: A and B (see Figure 1). Point A represents the end of the vertical portion of the nose and start of the rounding portion. Point B represents the ending of the rounding portion and start of the main vehicle body. In Figure 1 and further on in the paper the variable s represents the arc length along the cross section of the vehicle body starting from the center of the nose.

* VisualDOC Project Manager, Senior Member AIAA.

[†] Associate Research Engineer

[‡] Head, Structural Acoustics Department

[§] Professor of Mechanical and Industrial Engineering, Senior Member AIAA.

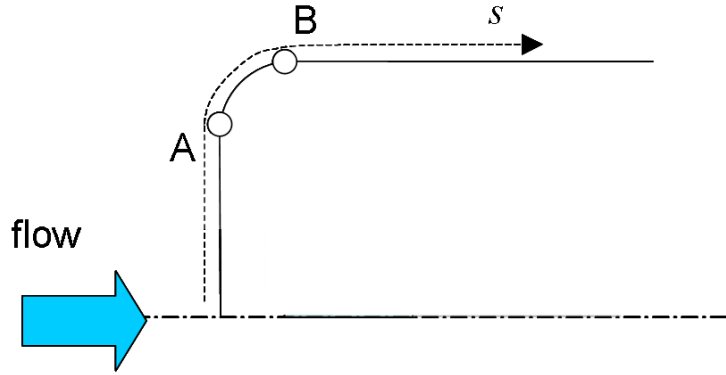


Figure 1. Schematic representation of an axisymmetric vehicle nose

The Transition Analysis Program System (TAPS)² code was used to calculate the desired flow performance characteristics: location of the boundary layer transition point, $t(s)$, location of the laminar separation point, $l(s)$, pressure coefficient, C_p , and gradient of C_p with respect to the arc length s over body, $\Delta C_p/\Delta s$. The primary program components of TAPS include body geometry, potential flow, boundary layer analysis, and stability analysis. The potential flow code computes the pressure distribution over the body surface for a given Reynolds number, Re . The boundary layer profiles are then computed at each body location until laminar separation occurs. After that the stability analysis predicts the growth rates of the boundary layer disturbances at specified non-dimensional frequencies. Transition from laminar to turbulent flow is said to occur when the disturbance amplification, $\ln(A)$ reaches a value of 9 at any given frequency.

III. Nose Shape Representation via Ellipsoid

In our first approach to the nose shape optimization the rounding of the nose was represented by an ellipsoid constructed using two control points A and B. These points define the two main axes of the ellipsoid. Changes in the main axes of the ellipsoid reflect the changes of the nose shape. Figure 2 presents more details on defining the flow over the modified nose geometry where potential modifications are defined via the ellipsoid. The “Laminar separation” notation in Figure 2 indicates where laminar separation of the boundary layer takes place downstream of the transition point.

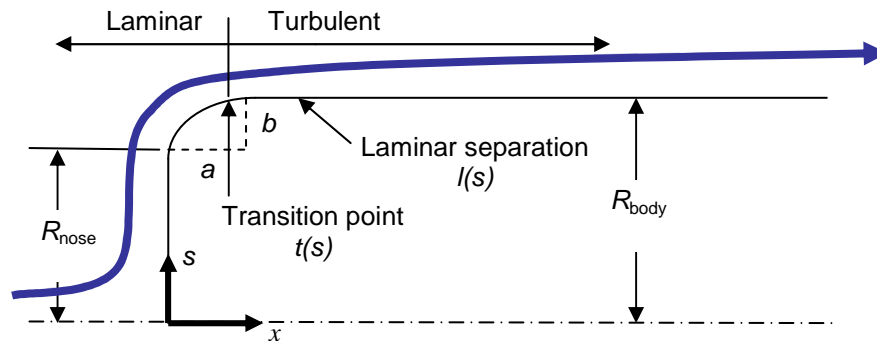


Figure 2. Vehicle nose shape optimization problem definition with rounding specified via ellipsoid

A. Extracting Analysis/Simulation Results

Figures 3-5 show typical TAPS results for the axisymmetric vehicle nose problem. The body geometry and potential flow solution are shown in Figure 3. Figure 4 shows the peak in the pressure coefficient gradient, $\Delta C_p/\Delta s$, and its location relative to the minimum value of the pressure coefficient, $C_{p\min}$. Figure 5 shows the transition point location for the body geometry and given Reynolds number, Re . Identifying the location of the transition point requires some effort as the amplification curves for several non-dimensional frequency ranges have to be analyzed.

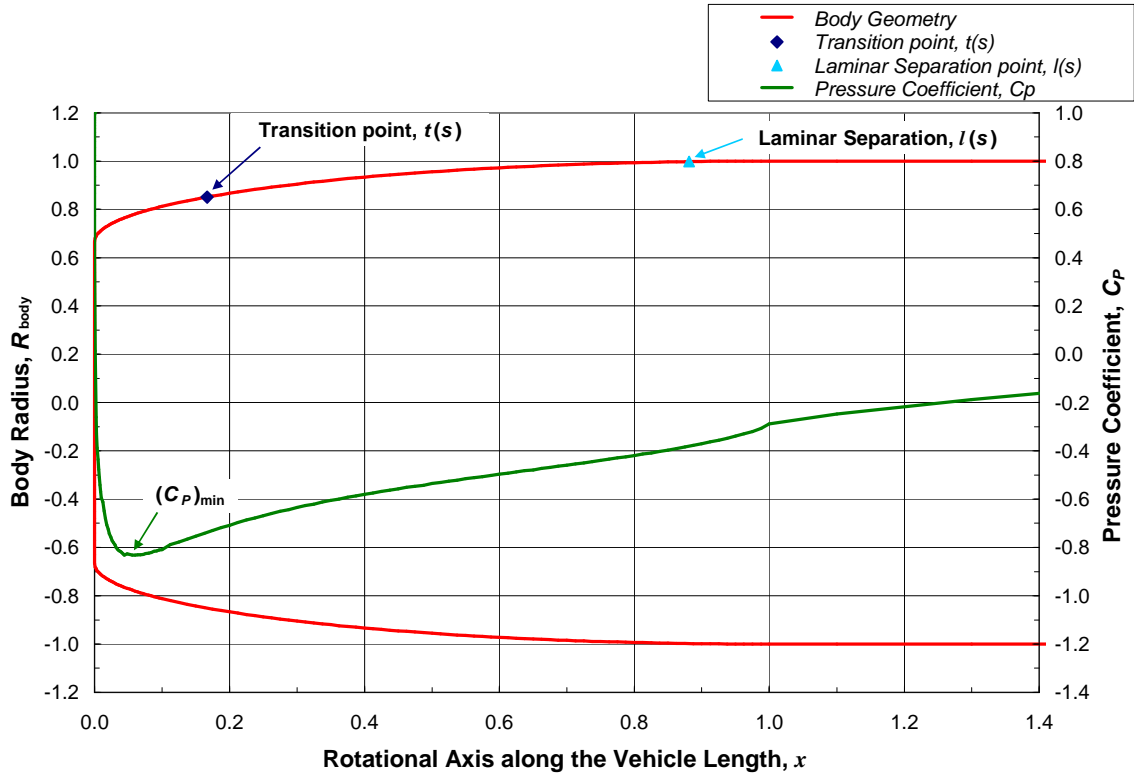


Figure 3. Typical C_p distribution and location of the transition and separation points on the vehicle body as a result of TAPS analysis

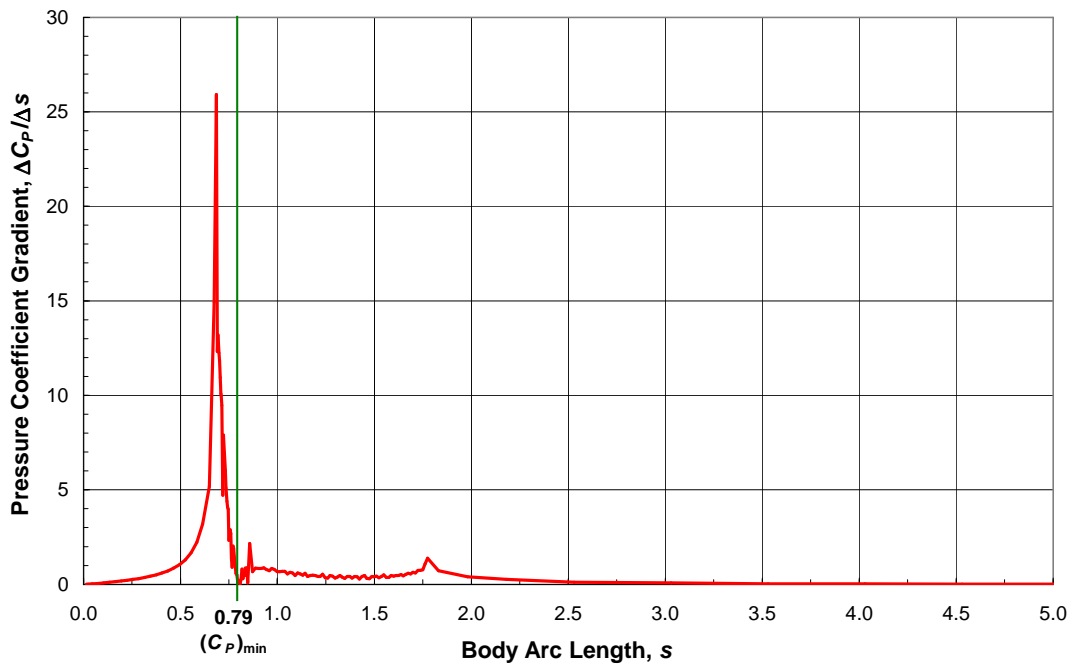


Figure 4. Typical C_p gradient values along the body arc length as a result of TAPS analysis

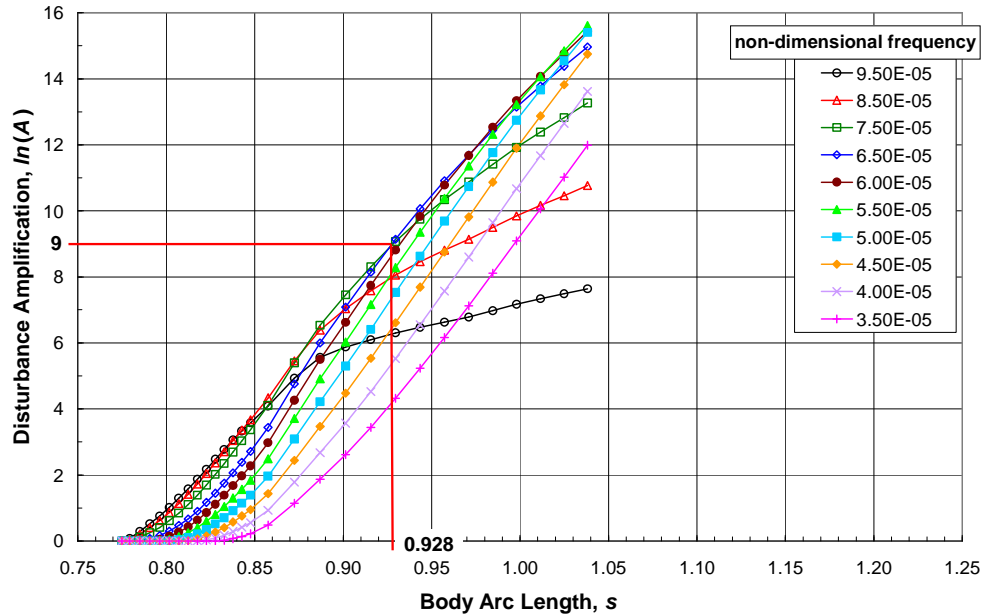


Figure 5. Example of identifying the location of a transition point (0.928) from disturbance growth rates using TAPS stability analysis

B. Optimization Problem Statement

Geometrical conditions: R_{body} is fixed

$$R_{\text{nose}} = R_{\text{body}} - b$$

Design variables: $0.3 < a < 3$
 $0.3 < b < 0.96$

Possible objective functions:

Maximize transition point location: $t(s)$

Minimize value of $C_{p_{\text{min}}}$

Minimize peak (maximum) value of $\Delta C_p / \Delta s$

The reason for selecting these particular objectives is the following:

- Moving the transition point as far downstream as possible reduces the spatial extent of the turbulence acting on the surface
- Minimizing the minimum of the pressure coefficient, $C_{p_{\text{min}}}$, typically minimizes cavitation
- Minimizing $\Delta C_p / \Delta s$ reduces the strength of the turbulence acting on a surface

In addition to the size constraints on the variables, the performance constraint was established to make sure that the laminar separation point is downstream of the transition point.

C. Single Objective Optimization Problem Results

Three variations of the optimization problem were performed. Each variation represented a single-objective optimization problem that used one of the three identified objectives, while the other two objectives were not considered. Thus the best possible result for the specific objective was obtained without the influence of the other objectives. The optimizations were performed using VisualDOC³ software from Vanderplaats R&D, Inc.

We employed several optimization methods. Table 1 summarizes the results for the Response Surface optimization method. This method in most cases required the least number of analyses to get to the region of the optimum. Table 1 shows the results of optimizing for different objectives. The objective function used in the specific optimization is presented in the first column. The first row in Table 1 represents the initial design from where all optimizations were started.

Table 1. Optimization results for single-objective problems with nose shape represented via ellipsoid

	a	b	$t(s)$	$C_{p_{\min}}$	Max $\Delta C_p/\Delta s$
Initial design	1.00	.33	.92	-0.85	23.19
Max transition, $t(s)$	1.94	.96	1.85	-.33	1.91
Min ($C_{p_{\min}}$)	3.00	.30	.72	-2.43	126.36
Min Max($\Delta C_p/\Delta s$)	1.82	.96	1.84	-.35	1.86

The results indicate that maximizing the location of the transition point and minimizing the peak of the C_p gradient result in a similar design, both in terms of the resultant values of the design variables and performance characteristics. On the other hand, minimizing the value of $C_{p_{\min}}$ results in a significantly different design. It is the designer's responsibility to then decide which type of design to use.

One of the ways to resolve this situation is with the help of experienced designers to identify which objective is most important, while putting constraints on the other responses with reasonable limits. Below is one of the possible optimization problem formulations used to achieve this:

Minimize: $C_{p_{\min}}$
 Subject to: $\Delta C_p/\Delta s < 12$
 Transition point $t(s) > 1.1$

The design variables used were the same as in the previous optimization problems. The optimization results are presented in Table 2.

Table 2. Results of compromised optimization with nose shape represented via ellipsoid

	a	b	$t(s)$	$C_{p_{\min}}$	Max $\Delta C_p/\Delta s$
Initial design	1.00	.33	.92	-.85	23.19
Min ($C_{p_{\min}}$)	0.68	.81	1.30	-1.09	8.27

The new results represent a compromise between various objective values from Table 1. However, the value of the design variable a is different from any of the optimum results in Table 1. In our experience the most reasonable explanation to such a situation is a relative flatness of the design space with respect to variable a , which means that there is a small sensitivity of the objective with respect to this particular variable.

D. Multi-Objective Exploration

In addition to single-objective optimization, a study was performed to indirectly confirm the optimization results and to visualize the trade-off between the three objectives. The visualization and multi-objective optimization work was performed using the Trade Space Visualization Software (ATSV)⁴ software from the Pennsylvania State University. To perform this study, 1000 random points were analyzed within the design space defined by the bounds on the two design variables.

Figure 6 represents these 1000 points in the objective functions space. Pareto Points were identified among the 1000 points to get the visual representation of the trade-off between various objective functions. This approximate Pareto Front in objective functions space is represented in Figure 7. Figure 7 confirms the conclusions drawn from the single objective optimization study: maximizing the location of the transition point and minimizing the peak of the Cp gradient resulted in similar designs, while minimizing Cpmin yields a design with markedly different performance characteristics.

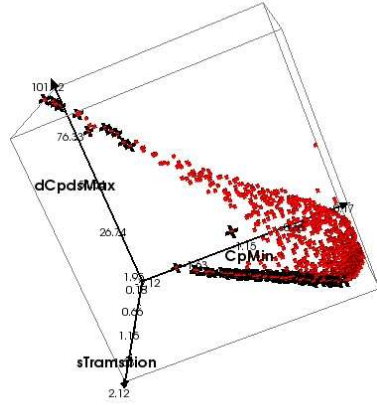


Figure 6. Exploration of the design space in the objective functions space with nose shape represented via ellipsoid

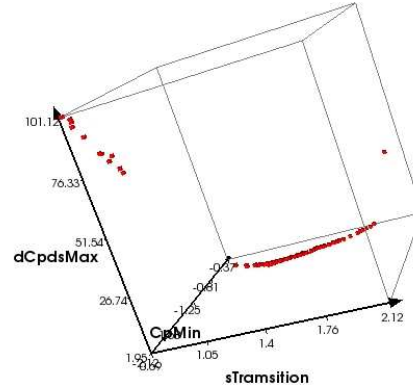


Figure 7. Approximate Pareto Front in the objective functions design space with nose shape represented via ellipsoid

IV. Nose Shape Representation via Ellipsoid and Hicks-Henne Functions

To investigate possible further improvements in flow characteristics, variations in the possible nose shapes geometries were expanded. Two areas were explored simultaneously. First, the bounds on the design variables (a and b) were expanded. Table 1 shows that the optimum design that minimizes $C_{p_{min}}$ is located on the boundary of the considered design space. It is reasonable to expand the bounds slightly to explore the new design space. The second area of design study was the exploration of the new representation of the nose shape. Using a weighted sum of shape functions (detailed below) superimposed on the ellipsoid to represent the nose shape provided additional opportunities for exploring the design space. As the Hicks-Henne shape functions were successfully used for representing the shape of 2-D airfoils^{5,6}, the authors felt that they could be successfully utilized for our problem also.

In the present paper the Hicks-Henne shape functions were used as follows: the geometric shape was represented as the weighted sum of the shape functions:

$$Y = Y_{base} + \sum_i W_i F_i \quad ,$$

where Y_{base} is the baseline function (an ellipsoid for this case), W_i is a weight factor for the specific shape function F_i , and F_i is a shape function. In the present paper we used the five following shape functions:

$$F_1 = [\sin(\pi x^{0.3})]^6, \quad -0.20 \leq W_1 \leq 0.001$$

$$F_2 = [\sin(\pi x^{0.5})]^3, \quad -0.35 \leq W_2 \leq 0.005$$

$$F_3 = [\sin(\pi x^{0.8})]^3, \quad -0.37 \leq W_3 \leq 0.22$$

$$F_4 = [\sin(\pi x^{1.357})]^3, \quad -0.31 \leq W_4 \leq 0.1$$

$$F_5 = [\sin(\pi x^{3.0})]^3, \quad -0.12 \leq W_5 \leq 0.02$$

These five normalized shape functions are presented in Figure 8. The power coefficients and the bounds on the weight factors were chosen from experimenting with the shapes that the functions produced for our specific problem.

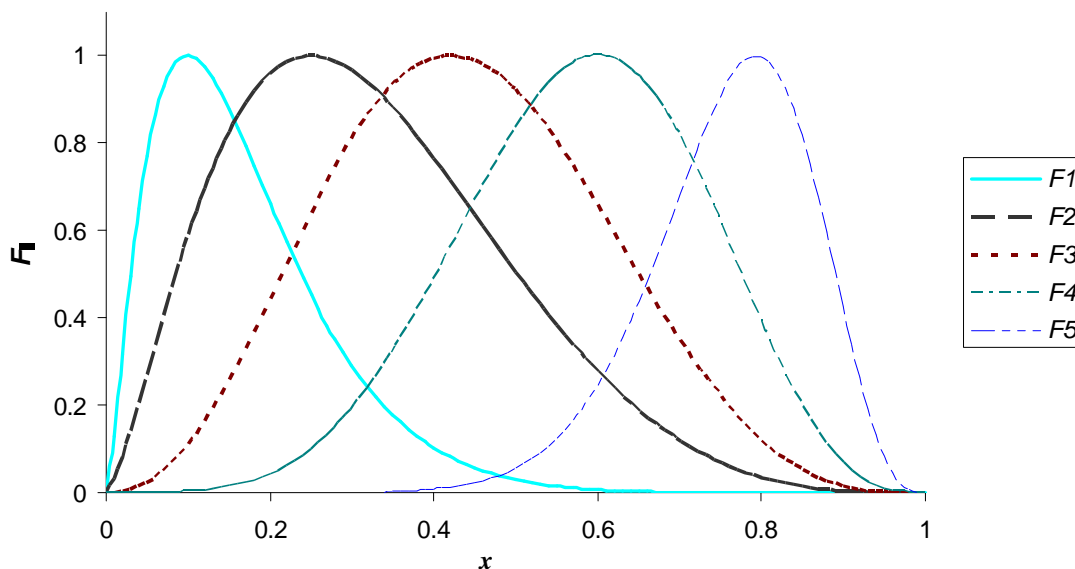


Figure 8. Normalized Hicks-Henne functions used in this study

A. Optimization Problem Statement

The previous optimization studies showed that minimizing maximum value of $\Delta C_p/\Delta s$ resulted in similar nose shapes to maximizing the location of the transition point. As a result, the new studies restrict the single-objective optimizations to two problems: maximizing the transition point location and minimizing the value of $C_{p_{\min}}$. The bounds on the ellipsoid parameters were also expanded. The optimization problems were formulated as follows:

Geometrical conditions: R_{body} is fixed

$$R_{\text{nose}} = R_{\text{body}} - b$$

Design variables:

- $0.1 < a < 5$
- $0.1 < b < 0.96$
- $-0.2 < W_1 < 0.001$
- $-0.35 < W_2 < 0.005$
- $-0.37 < W_3 < 0.22$
- $-0.31 < W_4 < 0.1$
- $-0.12 < W_5 < 0.02$

Objective functions:

Maximize transition point location $t(s)$

Minimize $-C_{p_{\min}}$

Thus, the new optimization problem formulation had seven design variables instead of two, when the nose shape was represented by an ellipsoid only. Similarly to the previous optimization problem, an additional performance constraint was established to make sure that the laminar separation point was downstream of the transition point.

B. Single-Objective Optimization Problem Results

Two optimization problems were solved. Each problem represented a single-objective optimization problem that contained one of the two identified objectives, while the other was ignored. The optimizations were performed using VisualDOC software from Vanderplaats R&D, Inc. The weight factor design variables corresponding to the Hicks-Henne functions provided more flexibility to the design, and therefore, helped to improve the values of the individual objective functions. However, this flexibility came at the expense of the existence of many local optima. To overcome this situation, a Particle Swarm evolutionary algorithm was employed.

Table 3 summarizes the results of all optimizations performed, including the optimizations, when the nose shape was represented via an ellipsoid only. For the latter case the weight factor values in the table are set to zero. The first column in Table 3 specifies the objective functions used in the specific optimization. The first row in Table 3 represents the initial design from where all optimizations were started.

Table 3. Optimization results for all single-objective problems

	a	b	W_1	W_2	W_3	W_4	W_5	$t(s)$	$C_{p_{\min}}$	$\text{Max}(\Delta C_p/\Delta s)$
Initial design	1.00	.33	0	0	0	0	0	0.92	-.85	23.19
Max transition, $t(s)$ 2 variables	1.94	.96	0	0	0	0	0	1.85	-.33	1.91
Min ($C_{p_{\min}}$) 2 variables	3.00	.30	0	0	0	0	0	.72	-2.43	126.36
Min $\text{Max}(\Delta C_p/\Delta s)$ 2 variables	1.82	.96	0	0	0	0	0	1.84	-.35	1.86
Max transition, $t(s)$ 7 variables	3.48	.96	-.031	-.097	-.090	.020	.020	2.96	-.27	16.65
Min ($C_{p_{\min}}$) 7 variables	2.91	.33	-.015	-.031	-.030	.001	-.003	.67	-6.80	650.00

The values in boldface type in Table 3 represent the objective function values achieved using two design variables vs. values achieved using seven design variables. Figure 9 represents the shapes of all the bodies from Table 3.

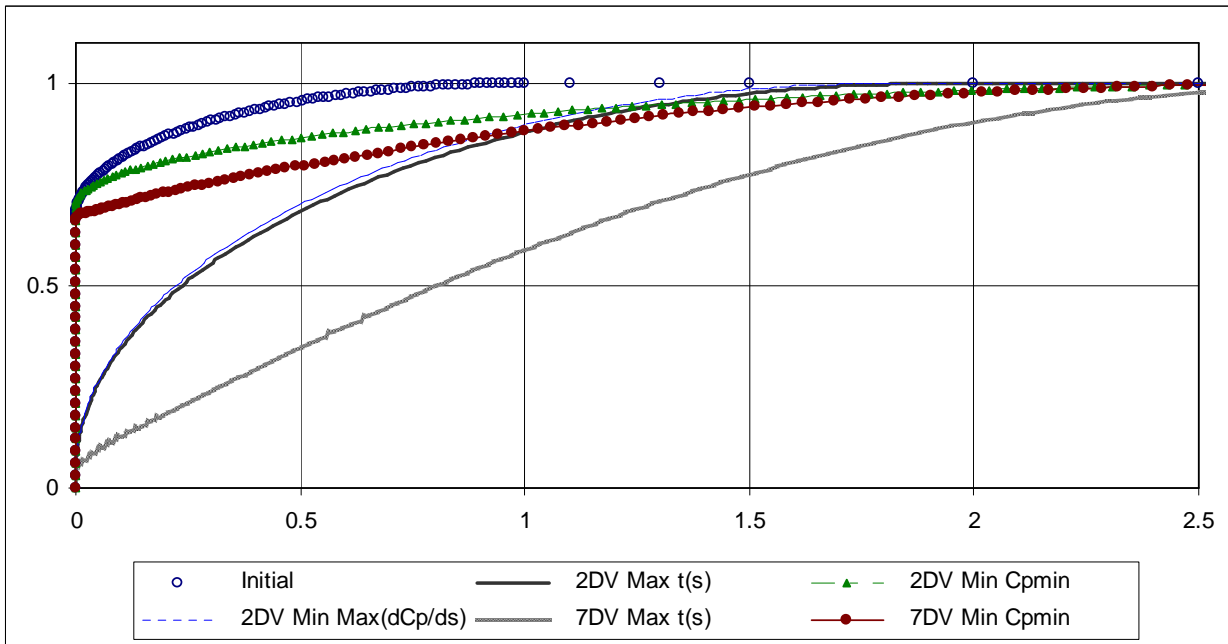


Figure 9. Shapes for all the designs represented in Table 2

Common trends are observed when considering the results in Table 3 and Figure 9. The designs that maximize the transition point location tend to have a small vertical portion at the nose (the lines without markers in Figure 9), whereas the designs that minimize $C_{p_{\min}}$ tend to have a relatively large vertical nose portion with a relatively “sharp corner,” then remains relatively “flat” as it transitions into the vehicle body (the lines with the markers in Figure 9).

C. Multi-Objective Exploration

Similar to multi-objective study performed for the two-design variable problems, a study for a seven-design variable problem was performed. The visualization and multi-objective optimization work was performed using ATSV software. Figure 10 shows all the points analyzed in the process of all Particle Swarm optimizations, and Figure 11 shows the Pareto points extracted from all the points. Similar trends in Pareto points from Figure 7 and Figure 11 are noted. Figure 12 and Figure 13 show the relationship between all the variables and responses for all the analyzed points and for the Pareto Points only, respectively.

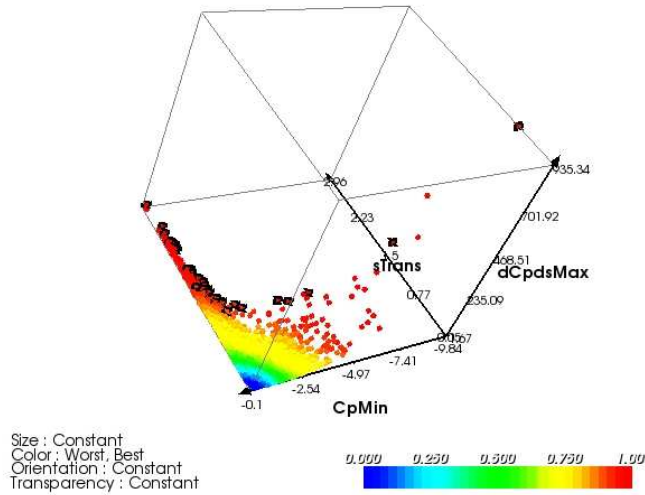


Figure 10. Plot of all the points visited during optimizations
(Color corresponds to points preference:
red – most preferred, blue – least)

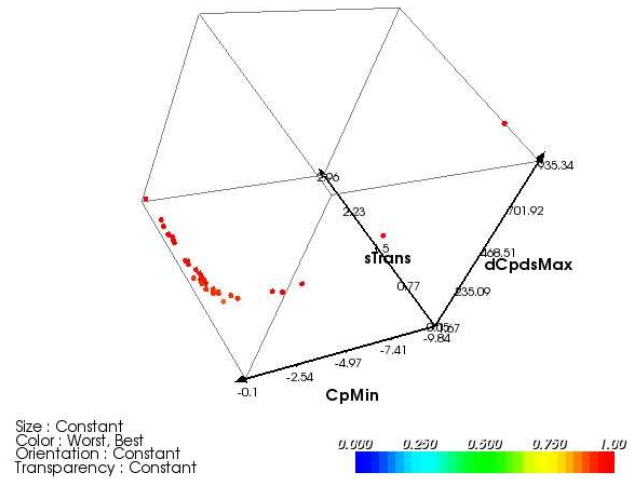


Figure 11. Pareto points extracted from all the points

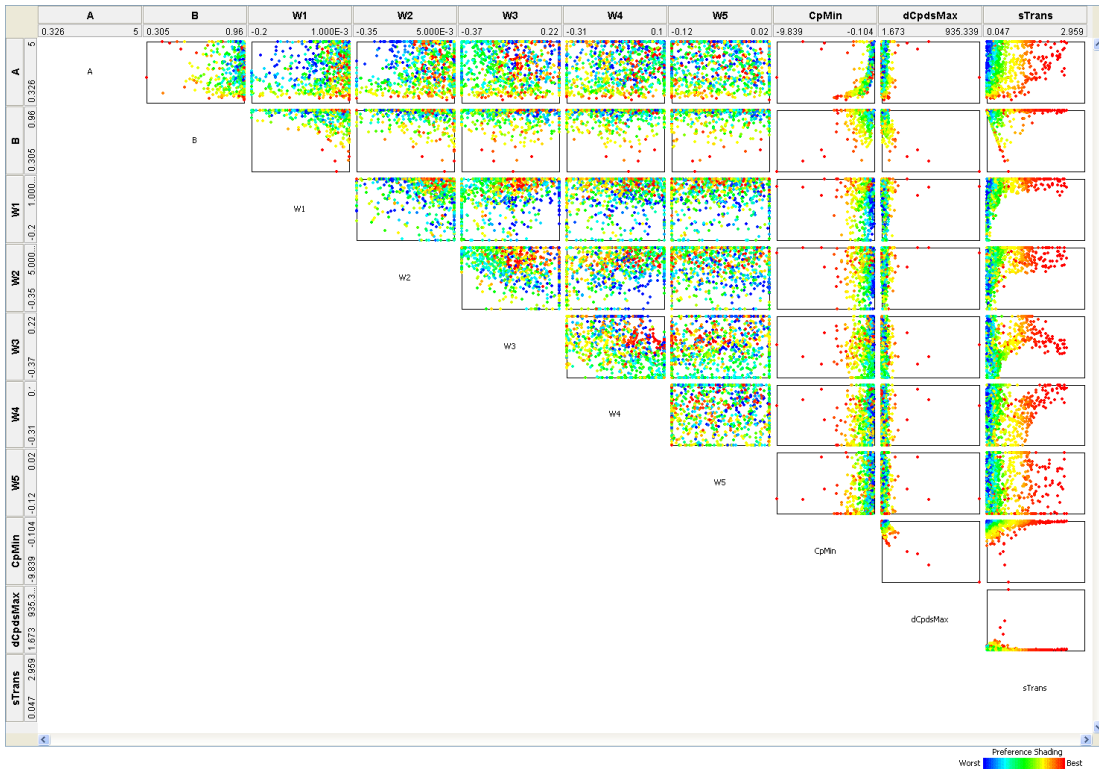


Figure 12. Scatter plot showing relations between all variables and responses (Color corresponds to points preference: red – most preferred, blue – least)

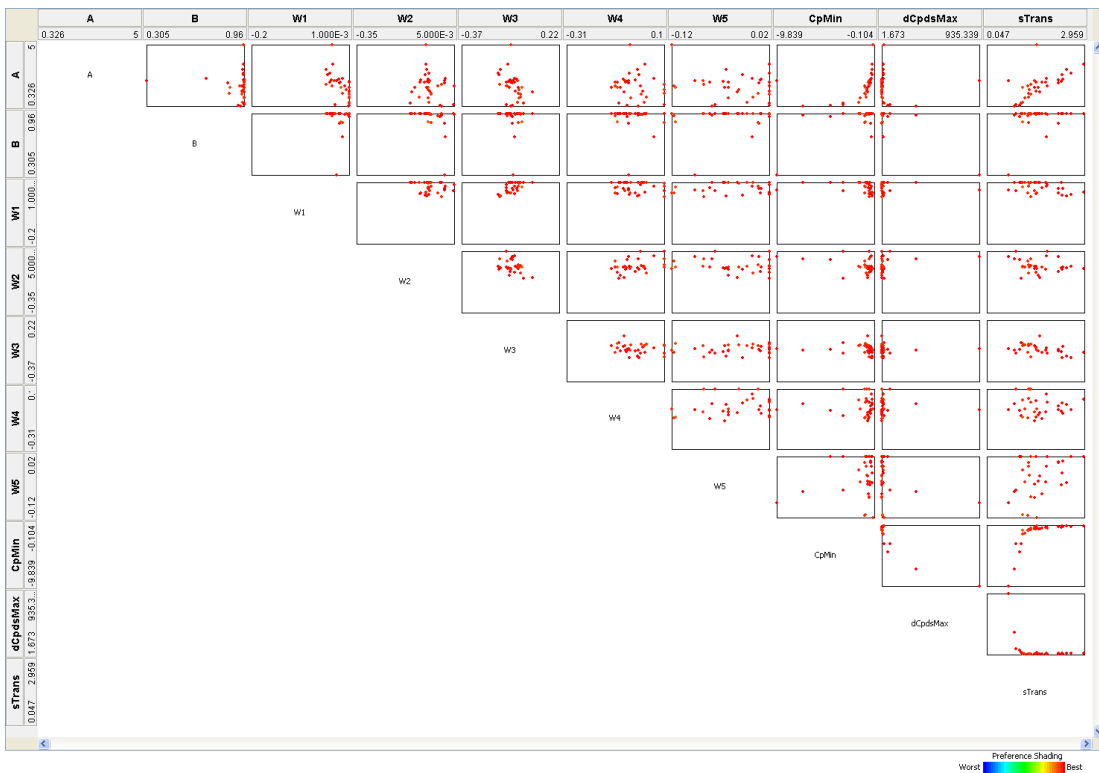


Figure 13. Scatter plot showing relations between all variables and responses for Pareto Points only

V. Concluding Remarks and Future Work

In this paper, we used optimization techniques to improve several flow characteristics of an axisymmetric vehicle by adjusting the vehicle's nose shape. The first part of the presented work optimized a more traditional representation of an axisymmetric vehicle nose (i.e., an ellipsoidal shape). The second portion expanded the design space by introducing Hicks-Henne functions to consider more variety in the nose shapes. Common trends in nose shape were identified for both approaches in terms of optimizing the vehicle's flow characteristics. The tradeoff studies presented illustrate how a designer can choose the nose shape dependent on his/her preferences. By visualizing the Pareto points, it should be easier for a designer to identify tradeoffs between desired characteristics. Introducing more flexibility into the nose shape geometry resulted in improving the individual flow characteristics, but also introduced difficulties for more traditional optimization techniques (i.e., Gradient-based optimization and Response Surface optimization).

Future work may focus on further study of Hicks-Henne functions for this particular application, increasing the number of shape functions employed as well as adjusting their power coefficients. There is also a possibility to consider power coefficients of Hicks-Henne functions as design variables. Other computational, analytical, or empirical solutions for determining the nose shape may also be considered.

Acknowledgements

This work was supported in-part by a grant from the Office of Naval Research, Naval Sea Systems Command Contract No. N00014-07-M-0275, with Dr. Kam Ng (ONR Code 333) as contract monitor.

References

- ¹Arakeri, V. H., and Acosta, A. J., "Cavitation Inception Observations on Axisymmetric Bodies at Supercritical Reynolds Numbers," *Journal of Ship Research*, **20**(1), pp. 40-50, March 1976.
- ²Gentry, A. E., *The Transition Analysis Program System, Users Manual*, Naval Sea Systems Command, Report No. MDC J7255/01, June 1976.
- ³VisualDOC, Software Package, Ver. 6.0, Vanderplaats Research & Development, Inc., Colorado Springs, CO.
- ⁴Stump, G., Yukish, M., and Simpson, T. W., "The Advanced Trade Space Visualizer: An Engineering Decision-Making Tool," AIAA Paper 2004-4568.
- ⁵Hicks, R. and Henne, P., "Wing Design by Numerical Optimization," *Journal of Aircraft*, **15**(7), 1978, pp. 407-413.
- ⁶Reuther, J., "Aerodynamic Shape Optimization using Control Theory," NASA Technical Report NASA-CR-201064, 1996.